

- [15] W. Chai and D. Jiao, "Direct matrix solution of linear complexity for surface integral-equation-based impedance extraction of complicated 3-D structures," *Proc. IEEE*, vol. 101, no. 2, pp. 372–388, Feb. 2013.
- [16] T. Wan, Z. N. Jiang, and Y. J. Sheng, "Hierarchical matrix techniques based on matrix decomposition algorithm for the fast analysis of planar layered structures," *IEEE Trans. Antennas Propag.*, vol. 59, no. 11, pp. 4132–4141, Nov. 2011.
- [17] R. F. Harrington, "Boundary integral formulations for homogeneous material bodies," *J. Electromagn. Waves Appl.*, vol. 3, no. 1, pp. 1–15, Jan. 1989.
- [18] A. Vogt, H.-D. Brüns, H. Fielitz, and C. Schuster, "Modeling absorbing materials in cavities with apertures using the thin sheet approximation," in *Proc. Asia-Pacific Int. Symp. Electromagn. Compat. (APEMC)*, Melbourne, VIC, Australia, 2013, pp. 426–429.
- [19] A. J. Poggio and E. K. Miller, "Integral equation solutions of three-dimensional scattering problems," in *Computer Techniques for Electromagnetics*, R. Mittra, Ed. New York, NY, USA: Pergamon, 1973.
- [20] W. C. Chew, M. S. Tong, and B. Hu, *Integral Equation Methods for Electromagnetic and Elastic Waves*. San Rafael, CA, USA: Morgan & Claypool, 2007.
- [21] P. Ylä-Oijala, M. Taskinen, and J. Sarvas, "Surface integral equation method for general composite metallic and dielectric structures with junctions," *Prog. Electromagn. Res.*, vol. 52, pp. 81–108, 2005.
- [22] A. Heldring, J. M. Tamayo, and J. M. Rius, "On the degrees of freedom in the interaction between sets of elementary scatterers," in *Proc. IEEE 3rd Eur. Conf. Antennas Propag. (EuCAP)*, Berlin, Germany, Mar. 2009, pp. 2511–2514.
- [23] S. Börm, L. Grasedyck, and W. Hackbusch. (2013). *Hierarchical Matrices, Lecture Notes*. [Online]. Available: <http://www.mis.mpg.de/preprints/ln/lecturenote-2103.pdf>
- [24] W. Hackbusch, *Hierarchical Matrices: Algorithms and Analysis*, vol. 49. Berlin, Germany: Springer, 2015.
- [25] M. Bebendorf and S. Rjasanow, "Adaptive low-rank approximation of collocation matrices," *Computing*, vol. 70, no. 1, pp. 1–24, Feb. 2003.
- [26] S. Kurz, O. Rain, and S. Rjasanow, "Application of the adaptive cross approximation technique for the coupled BE-FE solution of symmetric electromagnetic problems," *Comput. Mech.*, vol. 32, nos. 4–6, pp. 423–429, Dec. 2003.
- [27] M. Bebendorf and S. Kunis, "Recompression techniques for adaptive cross approximation," *J. Integral Equ. Appl.*, vol. 21, no. 3, pp. 331–357, Sep. 2009.
- [28] M. Bebendorf, *Hierarchical Matrices: A Means to Efficiently Solve Elliptic Boundary Value Problems*. Berlin, Germany: Springer, 2008.
- [29] L. Grasedyck, "Adaptive recompression of  $\mathcal{H}$ -matrices for BEM," *Computing*, vol. 74, no. 3, pp. 205–223, May 2005.
- [30] R. F. Harrington and J. R. Mautz, "An impedance sheet approximation for thin dielectric shells," *IEEE Trans. Antennas Propag.*, vol. 23, no. 4, pp. 531–534, Jul. 1975.
- [31] J. A. Stratton, *Electromagnetic Theory* (International Series in Pure and Applied Physics). New York, NY, USA: McGraw-Hill, 1941.
- [32] VIA Technologies, Inc. (2001). *Mini-ITX Mainboard Specification White Paper*. [Online]. Available: <http://www.via.com.tw>
- [33] W. L. Stutzman and G. A. Thiele, *Antenna Theory and Design*. Hoboken, NJ, USA: Wiley, 2013.
- [34] F. Gronwald, "Antenna theory in resonating systems derived from fundamental electromagnetism," Inst. Grundlagen Elektrotechnik Elektromagnetische Verträglichkeit, Otto-von-Guericke Univ. Magdeburg, Magdeburg, Germany, habilitation thesis, 2006.
- [35] ANSYS, Inc., Canonsburg, PA, USA. (2014). *HFSS, Ver. 15.0.0*. [Online]. Available: <http://www.ansys.com>
- [36] ARC Technologies, Inc. *Technical Data Sheet, LS-10055*. [Online]. Available: <http://www.arc-tech.com>
- [37] N. Rahman, A. Sharma, and M. N. Afsar, "Characterization, design and optimization of low-profile cavities for UWB spiral antennas," *Int. J. Electromagn. Appl.*, vol. 2, no. 3, pp. 16–23, Aug. 2012.
- [38] A. Vogt, H.-D. Brüns, Q. Wu, F. Gronwald, and C. Schuster, "A measurement setup for quantification of electromagnetic interference in metallic casings," *IEEE Trans. Electromagn. Compat.*, vol. 57, no. 6, pp. 1354–1364, Dec. 2015.
- [39] R. Kriemann, " $\mathcal{H}$ -LU factorization on many-core systems," *Comput. Visualizat. Sci.*, vol. 16, no. 3, pp. 105–117, 2013.

## Multifunctional Microstrip Array Combining a Linear Polarizer and Focusing Metasurface

He-Xiu Xu, Shiwei Tang, Guang-Ming Wang, Tong Cai, Wanxia Huang, Qing He, Shulin Sun, and Lei Zhou

**Abstract**—Although microstrip reflectarrays/transmitarrays have been extensively studied in the past decades, most previous designs were confined to monofunctional operations based on either transmission or reflection. In this communication, we propose a scheme to design multifunctional arrays that can simultaneously exhibit the functionalities of a reflectarray and a transmitarray on the basis of the appealing feature of a polarizer we discovered (i.e., constant phase difference between its cross-polarization transmission and copolarization reflection within a broadband). To demonstrate the proposed scheme, we designed and fabricated a multifunctional device comprising a  $15 \times 15$  array of twisted complementary dual-split ring resonators, each carefully designed to exhibit the desired transmission phase satisfying a parabolic distribution. Feeding the device by a Vivaldi antenna at its focus, we numerically and experimentally demonstrated that our system functioned as a directive emitter working in a transmission/reflection mode for cross-polarization/copolarization radiation at low/high frequencies, and it can radiate directly in both directions with different polarizations at intermediate frequencies. The half-power beamwidth of the array antenna was  $\sim 15^\circ$ , which is  $40^\circ$  narrower than that of a bare Vivaldi antenna. Moreover, the gain was higher than 13 dB in all cases studied, which is at least 7 dB higher than that of the Vivaldi antenna.

**Index Terms**—Broadband, linear polarizer, metasurface, microstrip arrays, multifunctional.

### I. INTRODUCTION

Although reflectarrays [1], [2], or transmitarrays [3], have been proposed for decades, they still attract considerable interest from a wide range of scientists and engineers in recent years [4]. This is especially true for microstrip arrays; such arrays are composed of a planar array of printed elements on dielectric boards and thus exhibit the merits of high gain, light weight, low cost, and low profile, in addition to easy fabrication without the necessity of complex feeding networks relative to parabolic reflectors, phased-array antennas, and weighty-shaped dielectric lenses. Therefore, microstrip arrays are considered one of the most promising alternatives for satellite-based telecommunication systems and have undergone rapid growth over the past decades; the examples of such arrays include multilayer arrays for bandwidth enhancement or full  $2\pi$  phase control [5], tunable arrays for beam steering or frequency, polarization and radiation pattern reconfigurability [6], element-rotated arrays for circularly

Manuscript received November 2, 2015; revised April 23, 2016; accepted April 28, 2016. Date of publication May 10, 2016; date of current version August 2, 2016. This work was supported in part by the National Natural Science Foundation of China under Grant no. 11304002, Grant no. 61501499, Grant no. 61372034, and Grant no. 11474057, in part by the Natural Science Foundation of Shaanxi Province under Grant no. 2016JQ6001, and in part by the China Postdoctoral Science Foundation under Grant no. 2015M570323 and Grant no. 2016T90337.

H.-X. Xu is with the State Key Laboratory of Surface Physics and the Key Laboratory of Micro and Nano Photonic Structures (Ministry of Education), Fudan University, Shanghai 200433, China, and also with the Air Force Engineering University, Xi'an 710051, China (e-mail: hxuellen@gmail.com).

S. Tang, T. Cai, W. Huang, Q. He, S. Sun, and L. Zhou are with the State Key Laboratory of Surface Physics and the Key Laboratory of Micro and Nano Photonic Structures (Ministry of Education), Fudan University, Shanghai 200433, China (e-mail: phzhou@fudan.edu.cn).

G.-M. Wang is with Air Force Engineering University, Xi'an 710051, China. Color versions of one or more of the figures in this communication are available online at <http://ieeexplore.ieee.org>.

Digital Object Identifier 10.1109/TAP.2016.2565742

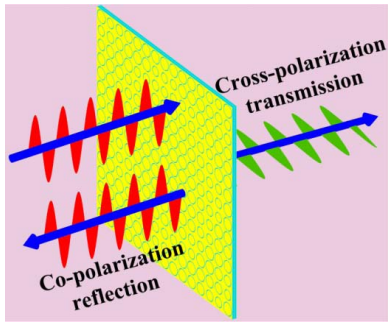


Fig. 1. Schematic of the functionality of the linear polarizer.

polarized waves [7], dualband/multiband [8] or multibeam arrays [9], dual reflectarrays for low cross polarization or low side lobes [10], and substrate integrated waveguide arrays for low profile [11].

Recently, abrupt phase discontinuities of a gradient metasurface (GMS) have been employed to demonstrate the generalized laws of reflection and refraction [12]. A set of functional devices [13]–[18] with wave bending, focusing, and even polarization control have been extensively studied from microwave [15]–[18] to terahertz regions [14], and even to IR/optical frequencies [12], [13], for their anomalous electromagnetic (EM) properties. Despite the progress achieved in both areas, multifunctionality with simultaneous focusing and polarization control still remains one of the most challenging problems. This is particularly true for the low conversion efficiency because of the fact that the majority of scattered light resides in the ordinary component [12]. To mitigate this problem, linearly polarized (LP) conversion [14] and linear-to-circular polarization conversion [15], [18] combining anomalous refraction have been realized using anisotropic GMSs. However, to the best of our knowledge, high-efficiency linear polarization conversion techniques incorporating focusing capabilities, in addition to integrated reflectarrays and transmitarrays, are rarely observed in the open literature. Here, we conceived and realized a multifunctional array by combining an ultrathin broadband linear polarizer and a focusing metasurface. A twisted complementary dual-split ring resonator (CDSRR) [19] constituted the basic elements we used, and dual functionality can be actualized at different frequencies by appropriately designing the phase profile along the metasurface. Moreover, we used fewer layers (two in this particular design) to achieve the required phase variation, which should advance the state of the art of the existing transmitarrays [5], [6].

## II. FUNDAMENTALS AND DESIGN

Cross-polarization radiation is commonly considered ineffectual in practical applications and is often purposely suppressed in many scenarios. Nevertheless, it may find the applications in bidirectional antennas (involving the composite functions of a reflectarray and a transmitarray) or even multifunctional antennas with the frequency-dependent radiation pattern selectivity providing reversed beam directions between cross-polarization and copolarization radiations. Therefore, the critical step to realize our scheme is to engineer an LP polarizer exhibiting forward cross-polarization or copolarization transmissions, and backward copolarization or cross-polarization reflections, and significantly suppress residual components (Fig. 1). An essential phenomenon of constant phase difference between both the components from a coupled mode theory [20] is presented subsequently.

Assume that our GMS polarizer is illuminated by a normally incident EM wave along the  $z$ -direction with polarization along the

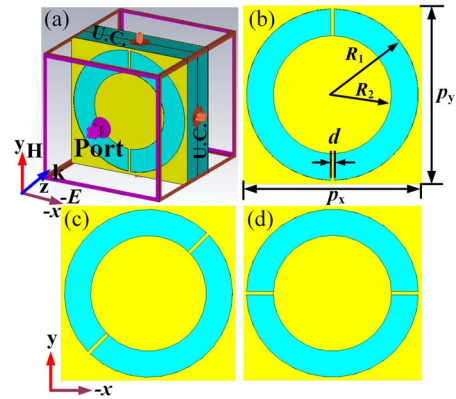


Fig. 2. Topology of the building block. (a) Perspective view. (b) Top layer. (c) Middle layer. (d) Bottom layer. The geometrical parameters are:  $p_x = p_y = 10$  mm,  $R_1 = 4.8$  mm,  $R_2 = 4.2$  mm, and  $d = 0.2$  mm. Here, theta is the angle between the axis normal to the meta-array plane and the beam direction.

$x$ -/ $y$ -axis, as shown in Fig. 2(a). Under the Cartesian coordinate system, forward transmitted (backward reflected) waves  $E_x^t$  ( $E_x^r$ ) and  $E_y^t$  ( $E_y^r$ ) are associated with incident waves  $E_x^i$  and  $E_y^i$  through four linear transmission (reflection) coefficients (complex Jones matrix)

$$\begin{pmatrix} E_x^r/t \\ E_y^r/t \end{pmatrix} = \begin{bmatrix} r/t_{xx} & r/t_{xy} \\ r/t_{yx} & r/t_{yy} \end{bmatrix} \begin{pmatrix} E_x^i \\ E_y^i \end{pmatrix}. \quad (1)$$

For an  $n$ th ports system without local resonance, input  $S_n^+$  waves are associated with outgoing waves  $S_n^-$  according to the following equation:

$$S_n^- = \sum_{n'} C_{nn'} S_{n'}^+ \quad (2)$$

where  $C$  denotes the transmission and reflection parameters ( $S$ -parameters) among different ports. Applying the time-reversal operation yields

$$S_n^+ = \sum_{n'} (C_{nn'})^* S_{n'}^-. \quad (3)$$

Substituting (3) into (2) yields

$$\sum_{n'} (C_{nn'})^* C_{n'n''} = \delta_{nn''}. \quad (4)$$

For  $x$  polarization, four LP components can be reduced to a two-port symmetric model with  $C = \begin{bmatrix} r & t \\ t & r \end{bmatrix}$  if  $|t_{xx}|$  and  $|r_{yx}|$  are negligible. Moreover, according to (4), we derive

$$\begin{aligned} C_{11}^* C_{11} + C_{12}^* C_{21} &= 1 \\ C_{11}^* C_{12} + C_{12}^* C_{22} &= 0. \end{aligned} \quad (5)$$

We can draw two conclusions from (5). One of the conclusions is for energy conversion ( $|r|^2 + |t|^2 = 1$ ), and the other is for  $r^*t + t^*r = 0$ , i.e.,  $\text{Re}(r^*t) = \text{Re}(e^{i(\varphi_t - \varphi_r)}) = 0$ . This indicates that an intrinsic phase relation  $\varphi_t - \varphi_r = 90^\circ / -90^\circ$  can be realized if both  $|t_{xx}|$  and  $|r_{yx}|$  can be completely suppressed.

### A. Topology and EM Property of the Element

To realize the aforementioned GMS polarizer, the unit cell structure (building block) should exhibit maximum  $|t_{yx}|$ , thus indicating no mirror symmetry. Therefore, a strong cross coupling ( $|t_{yx}|$ ) between electric and magnetic fields occurs at resonance, yielding chiral and bianisotropic effects. Fig. 2 shows the topology of the building

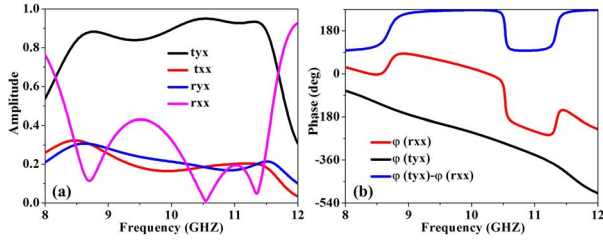


Fig. 3. Simulated transmission and reflection coefficients. (a) Amplitude. (b) Phase. The geometrical parameters are:  $p_x = p_y = 10$  mm,  $R_1 = 4.8$  mm,  $R_2 = 3.18$  mm, and  $d = 0.2$  mm.

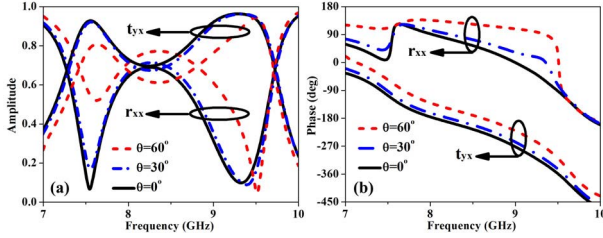


Fig. 4. Simulated transmission and reflection coefficients as a function of the elevation angle. (a) Amplitude. (b) Phase. The geometrical parameters are:  $p_x = p_y = 10$  mm,  $R_1 = 4.5$  mm,  $R_2 = 3.9$  mm, and  $d = 0.2$  mm.

block for our multifunctional array, indicating that it comprises three patterned metallic layers (copper with a thickness of 0.036 mm and a conductivity of  $\sigma = 5.8 \times 10^7$  S/m) separated by two dielectric layers. Each metallic layer has a sequentially rotated CDSRR with clockwise twist angles ( $\varphi$ ) of  $45^\circ$  from the top layer to the bottom layer. The dielectric spacer is an F4B substrate board with a dielectric constant ( $\epsilon_r$ ) of 4.5 and a thickness ( $h$ ) of 1.5 mm. The three CDSRRs couple with one another through two dielectric spacers.

To illustrate the unique EM properties of the GMS element, Fig. 3 shows the plots of the full-wave simulated transmission and reflection coefficients made through CST Microwave Studio, where unit cell boundary conditions are applied in the  $x$ - and  $y$ -directions to model an infinite slab. Fig. 3 shows that  $|t_{yx}|$  is inversely proportional to  $|r_{xx}|$  and is higher than 0.8 within 8.4–11.6 GHz, corresponding to a fractional bandwidth of 32%. Therefore, the forward cross-polarization transmission and backward copolarization reflection can be switched by altering the operating frequency. The three resonant peaks/dips in the  $|t_{yx}|/|r_{xx}|$  curve account for the broadband polarization conversion engendered by the superposition of multiple resonant modes of the three CDSRRs [14]. In addition, these resonances can be used to increase phase variations but with constant transmissions. Moreover,  $|t_{xx}|$  and  $|r_{yx}|$  are significantly suppressed with the approximate values of 0.2 within all observed frequencies and can be manipulated to be lower given a narrower slot width  $w = R_1 - R_2$ . In particular, the phase difference  $\Delta\varphi = \varphi_{t_{yx}} - \varphi_{r_{xx}}$  is expected to be constant at  $\sim 90^\circ/90^\circ$  in the nonresonant region of the entire  $x$ -band. This implies that using this type of element necessitates realizing only a parabolic phase profile for a reflectarray or transmitarray, with that for a residual array being fulfilled automatically. This is a highly appealing characteristic that is essential for the proposed multifunctional array design. In this design, a transmitarray also functions as a reflectarray given appropriate frequency-dependent  $|t_{yx}|$  and  $|r_{xx}|$ . This functionality can even be maintained for an oblique incidence with an elevation angle of up to  $45^\circ$ . This renders the proposed element a favorable candidate for high-gain arrays with

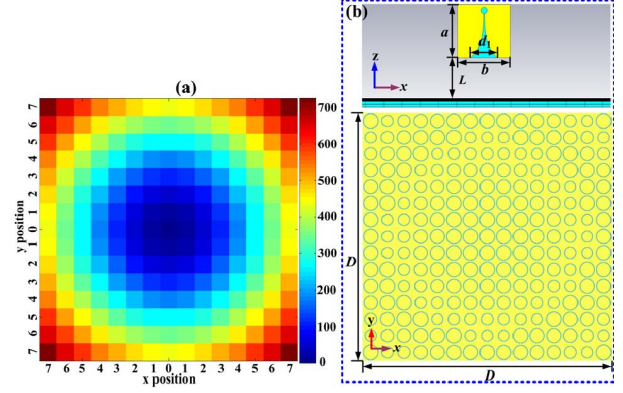


Fig. 5. (a) Phase distribution and (b) layout of proposed multifunctional array fed by a Vivaldi antenna. The geometrical parameters are  $a = 30$  mm,  $b = 30$  mm,  $L = 38$  mm,  $D = 150$  mm, and  $d_1 = 15$  mm.

small phase errors and offset-fed reflectarrays without feed blockage. However, for a wide-angle incidence up to  $60^\circ$ , the constant  $\varphi_{t_{yx}} - \varphi_{r_{xx}}$  and linear  $\varphi_{r_{xx}}$  cannot hold because of the increase in  $|t_{xx}|$  and  $|r_{yx}|$  (Fig. 4). An additional analysis and numerical study revealed that our anomalous polarizer can be converted into a common polarizer with  $|r_{yx}| \approx 1$  or  $|t_{xx}| \approx 1$  [16] by tuning the  $\varphi$  values of the three layers. Moreover, both the transmitted and reflected beams can be arbitrarily directed by arranging the nonuniform elements in an array with a linear phase gradient according to the generalized Snell's law [12]. Accordingly, the functionality can be generalized and the applications can be polarized in different scenarios.

### B. Antenna Structure and Design

The frequency-dependent  $|t_{yx}|/|r_{xx}|$  can be readily utilized to realize a multifunctional array with reflective, transmissive, and even bidirectional radiations at different frequencies. According to the unique feature described in Section II-A, we now concentrate on designing a parabolic phase profile distributed on the aperture (focusing metasurface). To maintain a constant phase difference between  $|r_{xx}|$  and  $|t_{yx}|$ , the GMS should be cautiously designed to avoid the resonant regions in the  $|t_{yx}|/|r_{xx}|$  curve. To efficiently collimate the outgoing wave from the feed and thus focus it on the  $xoz$  and  $yoz$  planes, the spatial phase  $\varphi(m, n)$  at element location  $(m, n)$  should be compensated by a phase delay  $\Delta\varphi(m, n) = \varphi(m, n) - \varphi(0, 0)$  accumulated from the feed to the GMS, yielding the following phase profile:

$$\Delta\varphi(m, n) = \frac{2\pi}{\lambda} \left( \sqrt{(mp)^2 + (np)^2 + F^2} - F \right) \quad (6)$$

where  $p$  and  $m$  and  $n$ , respectively, represent the periodicity and position of the GMS element along the  $x$ - and  $y$ -axes;  $F$  represents the focal length and  $\varphi(0, 0)$  represents the spatial phase at the center. Because the GMS can focus the incident plane wave to its focal point, a quasi-spherical wave emitted from a source placed at its focal point can also be collimated to a plane wave instead, enabling high directivity of a reflectarray/transmitarray. To efficiently collimate the spatial phase and thus achieve decent aperture efficiency, the maximum phase coverage must be greater than  $360^\circ$  along the  $x$ - and  $y$ -directions, and it is selected as  $[0^\circ, 726^\circ]$  in this particular design. Fig. 5 shows the antenna structure and corresponding calculated phase distribution, indicating that the meta-array (i.e., integrated linear polarizer and focusing metasurface) comprises an array of  $15 \times 15$  GMS elements and occupies an area of  $150 \times 150$  mm<sup>2</sup>.

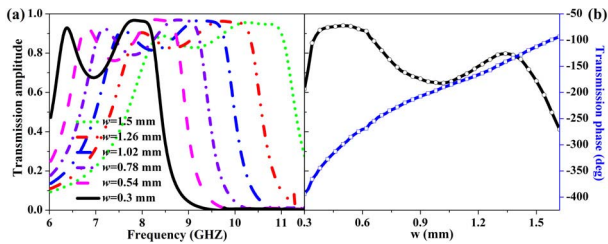


Fig. 6. Simulated  $t_{yx}$  of the GMS element as a function of  $w$ . (a) Magnitude response. (b) Magnitude and phase response at 8.25 GHz. The geometrical parameters are  $p_x = p_y = 10$  mm,  $R_1 = 4.8$  mm, and  $d = 0.2$  mm.

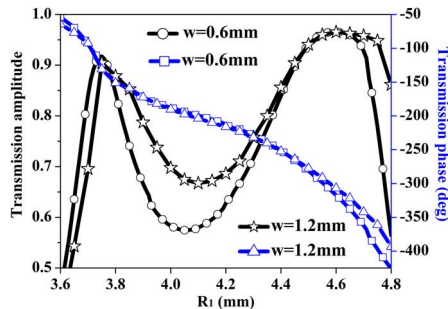


Fig. 7. Simulated  $t_{yx}$  of the GMS element as a function of  $3.6$  mm  $< R_1 < 4.8$  mm in the scenarios of  $w = 0.6$  mm at 9 GHz and  $w = 1.2$  mm at 10.26 GHz. Other geometrical parameters are  $p_x = p_y = 10$  mm and  $d = 0.2$  mm.

It is designed with a center frequency ( $f_0$ ) of  $\sim 9$  GHz and a focal length ( $F$ ) of 40 mm, and it is fed by a broadband Vivaldi antenna operated in the entire  $x$ -band. Therefore, the ratio of the focal length to the diameter is calculated as  $F/D = 0.267$ . The EM wave emitted from a Vivaldi antenna is an LP wave polarized along the  $x$ -direction; hence, the multifunctional array should be orthogonally oriented with the splits of CDSRR along the  $y$ -direction to ensure efficient excitation of the array. In addition, the feeding source is placed  $L = 38$  mm away from the fore end of the array in the final design by compensating the shifted phase center, and this is because the Vivaldi antenna is not an ideal point source. The phases along the GMS are discretized into  $15 \times 15$  grids and increase drastically with the radius because of the low  $F/D$ . In practical designs, all the phases with  $\Delta\phi(m, n) > 360^\circ$  are automatically deducted by  $360^\circ$ .

We next explored several possibilities to realize a GMS with a full  $360^\circ$  transmission phase variation by performing extensive parametric analyses. Fig. 6 shows the  $t_{yx}$  of the GMS element as a function of the slot width  $w$  when other parameters are kept constant. As expected, the operating frequency shifted upward significantly, and both the bandwidth dip and the transmission dip between two peaks increased progressively when  $w$  increased from 0.3 to 1.5 mm. The deterioration of the bandwidth as  $w$  decreased is attributable to the high  $Q$  factor of the element induced by the narrow slot, which can be explained by the high  $Q$  factor of thin metallic wires according to the Babinet principle. Nonetheless, the first peak  $|t_{yx}|$  decreased to a certain degree, resulting in deteriorated magnitude uniformity. Moreover,  $\phi t_{yx}$  covered a phase range of  $300.6^\circ$  with  $|t_{yx}| > 0.7$  when  $w$  changed within  $0.3$  mm  $< w < 1.62$  mm at 8.25 GHz. Therefore, this scanning strategy is not suitable for realizing a full  $360^\circ$  phase variation accompanied by a constant  $|t_{yx}|$  and bandwidth. Considering the magnitude, bandwidth, and phase span, we present another scanning strategy that entails tuning both  $R_1$  and  $R_2$  while keeping other parameters fixed (Fig. 7).

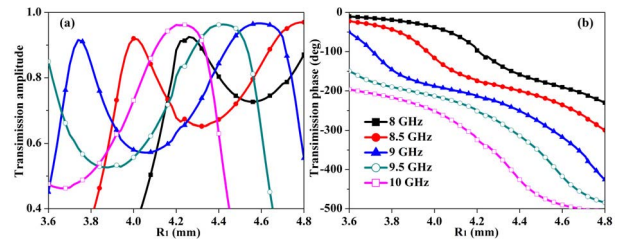


Fig. 8. Simulated (a) magnitude and (b) phase responses of  $t_{yx}$  as a function of  $R_1$  at 8, 8.5, 9, and 10 GHz. The geometrical parameters are  $p_x = p_y = 10$  mm,  $d = 0.2$  mm, and  $w = 0.6$  mm.

In this strategy, the transmission bandwidth at each  $R_1$  varies slightly, because  $w$  is constant. For a comprehensive study, we considered two scenarios. In the first scenario,  $w = 0.6$  mm, and in the second scenario,  $w = 1.2$  mm. As expected, the transmission dip reappeared and deteriorated as  $w$  decreased. The magnitude observed in the first scenario was  $|t_{yx}| > 0.56$ , whereas that observed in the second scenario was  $|t_{yx}| > 0.4$ . Furthermore, the phase exhibited a steeper slope in the first scenario, thus demonstrating a greater phase shift ( $359.5^\circ$ ) compared with that in the second scenario ( $329.3^\circ$ ). In short, the slot width should be sufficiently narrow to cover a full  $360^\circ$  phase range, but it should not be too narrow to have a moderate transmission magnitude; we thus subsequently set  $w$  to 0.6 mm in the design.

Notably, a change in gap  $d$  and element periodicity  $p_x$  induces a finite frequency shift and phase cover (considerably below  $360^\circ$ ) of  $t_{yx}$  along the metasurface (e.g., negligible upward frequency shift and slightly sharp phase variations as  $d/p_x$  increases/decreases). However, such a change can significantly affect the transmission/reflection performance (e.g., significantly reduced dip magnitude of  $|t_{yx}|$  as  $d$  or  $p_x$  increases). Therefore,  $d$  and  $p_x$  should be designed to sufficiently low values to engineer small in-band fluctuations of  $|t_{yx}|$  and high conversion efficiency. Consequently, we selected  $d = 0.2$  mm and  $p_x = p_y = 10$  mm in the final design.

The broadband characteristic of our GMS element is shown in Fig. 8, where  $|t_{yx}|$  and  $\phi t_{yx}$  are shown as a function of  $R_1$ . As shown in this figure, both  $|t_{yx}|$  and  $\phi t_{yx}$  underwent obvious shifts toward lower  $R_1$  values as the frequency increased from 8 to 10 GHz in the steps of 0.5 GHz, facilitating position-varied transmissions and larger accumulated interfacial phases. The case of  $f_0 = 9$  GHz exhibited two transmission peaks, whereas the residual cases demonstrated incompletely presented transmission peaks. A full  $360^\circ$  phase cover was observed at  $f_0$ , and the phase slope was flattened to a certain degree as  $f$  exceeded  $f_0$ , accounting for the minimum phase variation of  $220^\circ$  at 8 GHz. Nevertheless, the phase slopes were nearly parallel with one another in the 8–10-GHz frequency range, indicating that the array still operates efficiently with a moderate phase-collimating property. Beyond the operating band, the phase was almost the same at the lower edge of  $R_1$ , revealing the absence of a phase-collimating capability. On the basis of the preceding study, we could readily realize the phase profile shown in Fig. 4(a) and design the final array layout shown in Fig. 4(b) by conducting a geometrical mapping process by using the root finding algorithm and sweeping results shown in Fig. 7.

To intuitively predict the radiation functionality of our meta-array in the band defined by the phase-collimating property, Fig. 9 shows a plot of a simulated  $|t_{yx}|$  distribution and averaged  $|t_{yx}|$  and  $|r_{xx}|$  in the final aperture. As shown in this figure, a high  $|t_{yx}|$  value (more than 0.53) could be observed for each element at  $f_0 = 9$  GHz. When  $f < f_0$ , the  $T/R$  ratio improved progressively as  $f$  increased,

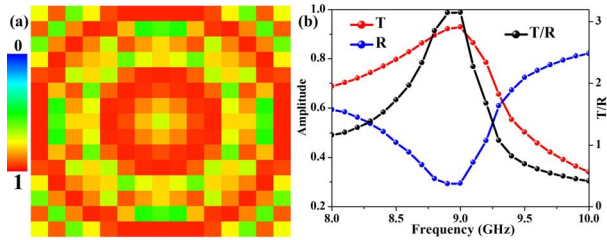


Fig. 9. (a) Simulated  $|t_{yx}|$  distribution at  $f_0 = 9$  GHz and (b) averaged  $|t_{yx}|$  ( $T = \sum |t_{yx}|/N$ ) and  $|r_{xx}|$  ( $R = \sum |r_{xx}|/N$ ) across the observed band.

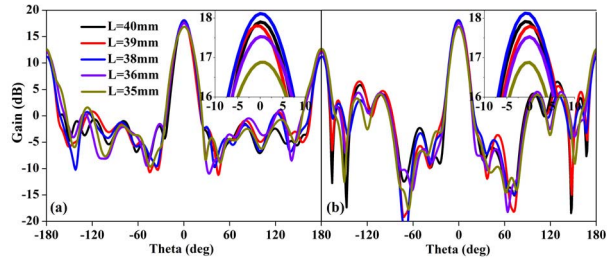


Fig. 10. Simulated radiation patterns of the multifunctional array at 9 GHz in (a)  $xoz$  ( $E$ ) plane and (b)  $yo z$  ( $H$ ) plane.

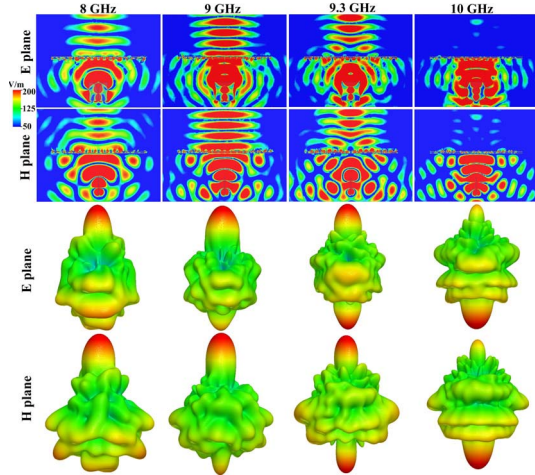


Fig. 11. Simulated  $E$ -field distributions (real parts) and radiation patterns (gain) of the meta-array at 8, 9, 9.3, and 10 GHz.

whereas when  $f > f_0$ , the ratio deteriorated as  $f$  increased, facilitating a near-complete transmission at  $f_0$ . Therefore, the transmitted peak gain of the resulting array is expected to be around  $f_0$ . Moreover, we can predict a forward radiation in the region before 9.3 GHz (intersection of the  $T$  and  $R$  curves), a bidirectional radiation in a certain band around 9.3 GHz, and a backward radiation after 9.3 GHz. Therefore, flexible functionality can be expected in a broadband with certain gain deterioration because of the blockage of the feed.

### III. NUMERICAL AND EXPERIMENTAL RESULTS

To validate our design, we evaluated the final array layout in HFSS. Fig. 10 shows the radiation patterns in two principal orthogonal planes (i.e.,  $xoz$  and  $yo z$ ) at 9 GHz. As described previously, the array presents an optimum gain of 18.3 dB in both the  $xoz$  ( $E$ ) plane and  $yo z$  ( $H$ ) plane when  $L = 38$  mm (effective  $F$  considering a nonideal phase center of the feeding source). The slightly higher side lobe in the  $H$ -plane than that in the  $E$ -plane is attributable to the

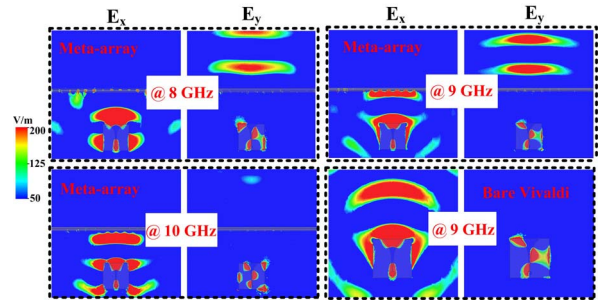


Fig. 12. Simulated  $E$ -field distributions (real parts) of the meta-array at 8, 9, and 10 GHz and those of the bare Vivaldi antenna at 9 GHz.

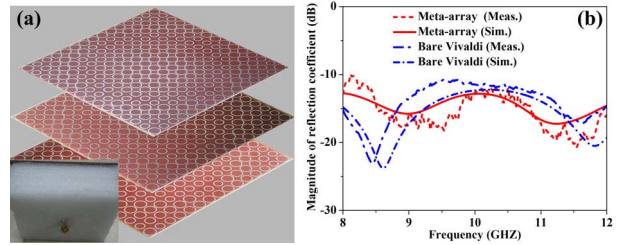


Fig. 13. (a) Photograph and (b) reflection coefficients of the fabricated multifunctional array. Inset: assembled array. The results of the bare Vivaldi antenna are presented for a clear comparison.

intrinsic asymmetric patterns of the feeding antenna in both planes. To intuitively demonstrate the functionality of our designed meta-array without loss of generality, we plot simulated  $E$ -field distributions and radiation patterns at four selected frequencies, as shown in Fig. 11. As illustrated in this figure, the wavefront outgoing from the array on both sides was flattened in both the  $E$ - and  $H$ -planes, clearly confirming the satisfactory focusing and collimating capability of the designed array. Slightly distorted and discontinuous wavefronts were observed below the meta-array, which are due to the effects of the feeding antenna whose radiation field interferes with the reflected EM wave. Moreover, the focusing effect deteriorated to a certain extent as the phases deviate from the ideal values. Therefore, the transmit field demonstrated the strongest and weakest intensity at 9 and 10 GHz, respectively, and decreased as the observed frequency departed from  $f_0$ . Consequently, the array exhibits clear forward radiations at 8 and 9 GHz, bidirectional radiation at 9.3 GHz, and completely backward radiation at 10 GHz. In short, we observed high consistency between the field distributions and the radiation patterns.

The  $E_y$  and  $E_x$  components at 8, 9, and 10 GHz in Fig. 12 provide more physical insight into the polarization-variable characteristic of our multifunctional array. Again, from the  $E_y$  distributions in the  $E$ -plane, the quasi-spherical wavefront outgoing from the Vivaldi antenna was successfully converted into a planar wavefront by the meta-array, further demonstrating the satisfactory focusing capability of this array. Furthermore, the radiation field outgoing from a bare Vivaldi antenna exhibits only an  $E_x$  component. However, this component was almost completely transformed into its orthogonal  $E_y$  counterpart by our multifunctional array, and no penetrated  $E_x$  component was observed, signifying a high polarization conversion efficiency.

To validate the aforementioned multifunctionalities of our meta-array, we fabricated a sample and measured it in an anechoic chamber (Fig. 13) to derive its photograph and reflection coefficients. Fig. 14 shows the  $E$ -plane and  $H$ -plane radiation patterns of the

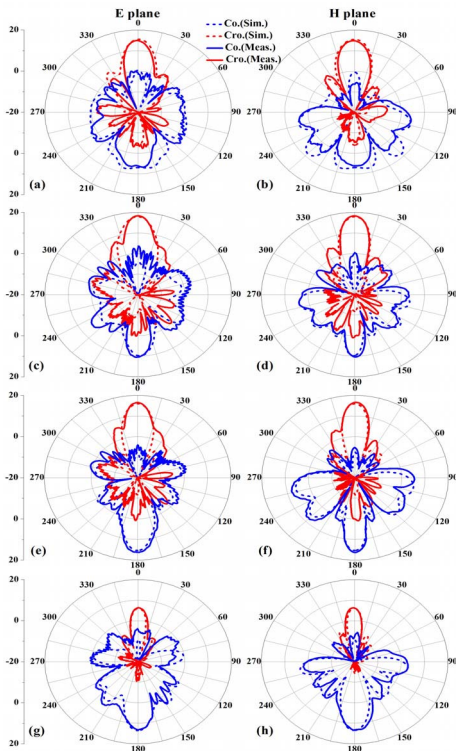


Fig. 14. Simulated and measured radiation patterns of the multifunctional array at (a) and (b) 8, (c) and (d) 9, (e) and (f) 9.3, and (g) and (h) 10 GHz, in  $E$ - and  $H$ -planes.

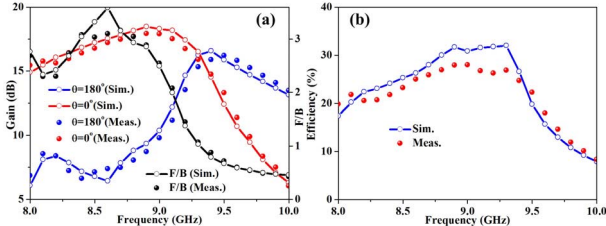


Fig. 15. Simulated and measured (a) gain and F/B and (b) aperture efficiency of the multifunctional array at  $\theta = 0^\circ$  and  $\theta = 180^\circ$ . The efficiency is calculated as the ratio between the gain (including both F/B radiations) and the maximum directivity [ $D = 4\pi S/(\lambda^2)$ ], where  $S$  is the area of the meta-array.

multifunctional array at 8, 9, 9.3, and 10 GHz. We observed that the simulated and measured results in all cases are reasonably consistent, thus further clearly validating the design effectiveness and functionality of our meta-array. Both the simulated and measured reflections were lower than  $-10$  dB over the entire  $x$ -band. The half-power beamwidth (HPBW) was nearly  $15^\circ$ , which was reduced by  $40^\circ$  relative to that of the bare Vivaldi antenna. The simulated and measured front-to-back ratio of the cross-polarization pattern was more than 17 dB. The deviations between the simulations and the measurements, particularly for the higher back and side lobes measured, can be attributable to the adhesives utilized for bonding the two substrates in the experiments. Nevertheless, this exerts few effects on the demonstrated functionality of the meta-array.

To further illustrate the in-band radiation characteristic at residual frequencies, Fig. 15 shows the simulated and measured gain and aperture efficiency from 8 to 10 GHz. Both the numerical and experimental results are highly consistent. The experimental results revealed that the array presented a peak forward/backward (F/B)

gain of nearly 18.5/13.1 dB at 8.9/10 GHz and a backward/forward gain at  $\sim 9.35/6.28$  dB. The 1-dB gain bandwidth was observed as 6.7%, and the measured/simulated antenna efficiency varied from 8.5% (10 GHz) to 28%/31% (9/9.3 GHz). The relatively low gain and the efficiency, particularly at the upper edge frequencies, are attributable to the bidirectional radiations and the low F/D ratio that engender high reflection phase errors of edge meta-atoms in terms of nonnormal incidence angles. High gain and aperture efficiency can be achieved by increasing the focal distance or by replacing the feeding antenna with a horn. However, this is not within the scope of this communication. The forward transmitted radiation ( $\theta = 0^\circ$ ) was higher/lower than the backward reflected radiation ( $\theta = 180^\circ$ ) within  $f \leq 9.2$  GHz/ $f \geq 9.5$  GHz; however, they exhibited almost the same intensity within  $9.3$  GHz  $\leq f \leq 9.4$  GHz. Therefore, our meta-array facilitates achieving a flexible frequency-dependent beam direction and radiation pattern diversity, namely, forward, bidirectional, and backward highly directive emissions at different frequencies. The maximum/minimum discrepancy between cross-polarization and copolarization patterns was 11.1/−6.8 dB at  $\sim 8.6/10$  GHz, yielding a peak/valley F/B ratio of 3.2/0.45.

#### IV. CONCLUSION

We conceived and realized a novel multifunctional array in the  $x$ -band by combining a broadband linear polarizer and a focusing metasurface. The appealing feature of constant phase relation between cross-polarization transmissions and copolarization reflections enables achieving an integrated functionality of a transmitarray and a reflectarray, or specifically radiation pattern diversity. The numerical and experimental results both demonstrate that the proposed multifunctional array cannot only switch the reflective, transmissive, or bidirectional radiation but also alter the polarization. The proposed strategy opens up an avenue to engineer multifunctional highly-directive antennas with radiation pattern diversity, thus demonstrating considerable potential applications in modern smart communication systems.

#### REFERENCES

- [1] D. G. Berry, R. G. Malech, and W. A. Kennedy, "The reflectarray antenna," *IEEE Trans. Antennas Propag.*, vol. 11, no. 6, pp. 645–651, Nov. 1963.
- [2] J. Huang and J. A. Encinar, *Reflectarray Antennas*. Hoboken, NJ, USA: Wiley, 2008.
- [3] D. M. Pozar, "Flat lens antenna concept using aperture coupled microstrip patches," *Electron. Lett.*, vol. 32, no. 23, pp. 2109–2111, Nov. 1996.
- [4] S. V. Hum and J. Perruisseau-Carrier, "Reconfigurable reflectarrays and array lenses for dynamic antenna beam control: A review," *IEEE Trans. Antennas Propag.*, vol. 62, no. 1, pp. 183–198, Jan. 2014.
- [5] B. Rahmati and H. R. Hassani, "Low-profile slot transmitarray antenna," *IEEE Trans. Antennas Propag.*, vol. 63, no. 1, pp. 174–181, Jan. 2015.
- [6] M. Sazegar *et al.*, "Beam steering transmitarray using tunable frequency selective surface with integrated ferroelectric varactors," *IEEE Trans. Antennas Propag.*, vol. 60, no. 12, pp. 5690–5699, Dec. 2012.
- [7] M. Zhou *et al.*, "The generalized direct optimization technique for printed reflectarrays," *IEEE Trans. Antennas Propag.*, vol. 62, no. 4, pp. 1690–1700, Apr. 2014.
- [8] R. S. Malfajani and Z. Atlasbaf, "Design and implementation of a dual-band single layer reflectarray in X and K bands," *IEEE Trans. Antennas Propag.*, vol. 62, no. 8, pp. 4425–4431, Aug. 2014.
- [9] P. Nayyeri, F. Yang, and A. Z. Elsherbeni, "Design and experiment of a single-feed quad-beam reflectarray antenna," *IEEE Trans. Antennas Propag.*, vol. 60, no. 2, pp. 1166–1171, Feb. 2012.
- [10] C. Tienda, J. A. Encinar, M. Arrebola, M. Barba, and E. Carrasco, "Design, manufacturing and test of a dual-reflectarray antenna with improved bandwidth and reduced cross-polarization," *IEEE Trans. Antennas Propag.*, vol. 61, no. 3, pp. 1180–1190, Mar. 2013.

- [11] M. Jiang, W. Hong, Y. Zhang, S. Yu, and H. Zhou, "A folded reflectarray antenna with a planar SIW slot array antenna as the primary source," *IEEE Trans. Antennas Propag.*, vol. 62, no. 7, pp. 3575–3583, Jul. 2014.
- [12] N. Yu *et al.*, "Light propagation with phase discontinuities: Generalized laws of reflection and refraction," *Science*, vol. 334, no. 6054, pp. 333–337, Oct. 2011.
- [13] X. Chen *et al.*, "Longitudinal multifoci metalens for circularly polarized light," *Adv. Opt. Mater.*, vol. 3, no. 9, pp. 1201–1206, 2015.
- [14] N. K. Grady *et al.*, "Terahertz metamaterials for linear polarization conversion and anomalous refraction," *Science*, vol. 340, no. 6138, pp. 1304–1307, 2013.
- [15] C. Pfeiffer and A. Grbic, "Millimeter-wave transmitarrays for wavefront and polarization control," *IEEE Trans. Microw. Theory Techn.*, vol. 61, no. 12, pp. 4407–4417, Dec. 2013.
- [16] H. Li, G. M. Wang, H.-X. Xu, T. Cai, and J. Liang, "X-band phase-gradient metasurface for high-gain lens antenna application," *IEEE Trans. Antennas Propag.*, vol. 63, no. 11, pp. 5144–5149, Nov. 2015.
- [17] T. Cai *et al.*, "Ultra-thin polarization beam splitter using 2-D transmissive phase gradient metasurface," *IEEE Trans. Antennas Propag.*, vol. 63, no. 12, pp. 5629–5636, Dec. 2015.
- [18] H. F. Ma, G. Z. Wang, G. S. Kong, and T. J. Cui, "Independent controls of differently-polarized reflected waves by anisotropic metasurfaces," *Sci. Rep.*, vol. 5, p. 9605, Apr. 2015.
- [19] Z. Wei, Y. Cao, Y. Fan, X. Yu, and H. Li, "Broadband polarization transformation via enhanced asymmetric transmission through arrays of twisted complementary split-ring resonators," *Appl. Phys. Lett.*, vol. 99, no. 22, p. 221907, 2011.
- [20] S. Fan, W. Suh, and J. D. Joannopoulos, "Temporal coupled-mode theory for the Fano resonance in optical resonators," *J. Opt. Soc. Amer. A*, vol. 20, no. 3, pp. 569–572, 2003.

## Gain Enhancement of Planar Antenna Enabled by Array of Split-Ring Resonators

Abdolmehdi Dadgarpour, Ahmed A. Kishk, and Tayeb A. Denidni

**Abstract**—This communication proposes a high-gain bow-tie antenna operating over the frequency band of 5.5–8 GHz. The proposed antenna is comprised of a microstrip-to-slot transition line connected to bow-tie radiators. Seven slabs of split-ring resonator (SRR) unit cells are integrated into the orthogonal plane of antenna substrate to enhance its gain. Each slab consists of  $2 \times 7$  double-sided SRR unit cells. A prototype of the antenna is fabricated and measured. The results indicate that the reflection coefficient is better than  $-10$  dB over the frequency band of 3.5–8 GHz. The measured antenna gain varies from 10.2 to 13.8 dBi over a frequency range of 5.65–7.8 GHz. The measured radiation efficiency corresponds to 90% at 7 GHz. The cross polarization is better than  $-30$  dB in the  $E$ -plane at 6.5 GHz.

**Index Terms**—Bow-tie antenna, end-fire antenna, gain enhancement, split-ring resonators (SRRs).

### I. INTRODUCTION

High-gain antennas have gained considerable attention as they can be deployed in indoor for high-data-rate wireless communication systems, such as high-definition video streaming and cellular base station, point-to-point, and long-range communications. Slot and microstrip antennas are suggested to achieve that. However, these antennas have a broadside radiation type, which is not appropriate for azimuthal beam-switching systems. End-fire antennas, such as Vivaldi and tapered slot antennas, are considered as promising candidates for this application [1], [2]. However, they occupy a large space and suffer from high cross polarizations, which restrict their applications. Yagi-Uda is another type of end-fire antenna, and lots of work have been undertaken to develop its radiation characteristics. For instance, a microstrip Yagi array design has been introduced in [3] to obtain a high gain more than 10 dBi and a low cross polarization over 30.8–33.5 GHz. However, the gain bandwidth is narrow, and the main beam direction in the  $E$ -plane changes with frequency, and its peak is tilted with respect to the end-fire direction. To increase the gain of the Yagi antenna, Kramer *et al.* [4] have reported a  $4 \times 4$  array of Yagi elements at millimeter wave as a stacked structure with a measured gain of 18 dBi over a 7% bandwidth. Nevertheless, this structure suffered from a narrowband gain bandwidth, and its multilayer design makes it complicated and costly for fabrication and integrating with monolithic integrated circuits. An end-fire antenna suitable for switched-beam systems at millimeter-wave bands made of a seven-element Yagi-Uda antenna has been proposed in [5] with a measured gain of 9–11 dBi over 22–26 GHz and a cross polarization of better than  $-16$  dB. However, the proposed antenna has a narrow gain bandwidth, and the protrusion dimension of the antenna in the end-fire direction corresponds to  $0.92\lambda_0$  at 22 GHz, which is too large.

Manuscript received February 29, 2016; revised April 24, 2016; accepted April 28, 2016. Date of publication May 10, 2016; date of current version August 2, 2016.

A. Dadgarpour and A. A. Kishk are with the Electrical and Computer Engineering Department, Concordia University, Montreal, QC H3G 1M8, Canada (e-mail: mehdidadgar60@gmail.com; kishk@encs.concordia.ca).

T. A. Denidni is with the Energy, Materials and Telecommunications Center, Institut National de la Recherche Scientifique, University of Quebec, Montreal, QC H5A 1K6, Canada (e-mail: denidni@emt.inrs.ca).

Color versions of one or more of the figures in this communication are available online at <http://ieeexplore.ieee.org>.

Digital Object Identifier 10.1109/TAP.2016.2565741